



Atmospheric observation-based estimation of fossil fuel CO₂ emissions from regions of central and southern California



Xinguang Cui ^{a,*}, Sally Newman ^{b,1}, Xiaomei Xu ^c, Arlyn E. Andrews ^d, John Miller ^d, Scott Lehman ^e, Seongeun Jeong ^a, Jingsong Zhang ^f, Chad Priest ^f, Mixtli Campos-Pineda ^f, Kevin R. Gurney ^g, Heather Graven ^h, John Southon ^c, Marc L. Fischer ^a

^a Lawrence Berkeley National Lab, Berkeley, CA, USA

^b California Institute of Technology, Pasadena, CA, USA

^c University of California Irvine, Irvine, CA, 92697, USA

^d Global Monitoring Division, NOAA Earth System Research Laboratory, Boulder CO, USA

^e University of Colorado, Boulder, CO, USA

^f University of California Riverside, Riverside, CA, USA

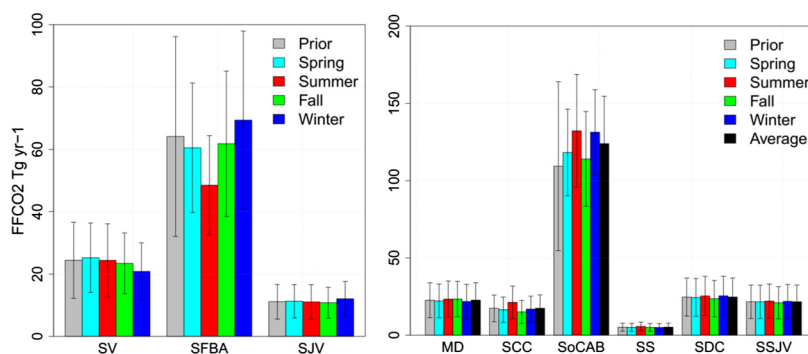
^g Arizona State University, Tempe, AZ, USA

^h Imperial College London, London, UK

HIGHLIGHTS

- Atmospheric fossil CO₂ enhancements estimated using ¹⁴CO₂ in central and southern California.
- Inversions suggest emissions within 10 ± 30% (at 95% confidence) of CARB inventory.
- Seasonal variations detected in the San Francisco Bay Area but not southern California.
- Inter-annual variation or trend is not significant in SFBA.
- Additional observations are needed to refine these estimates.

GRAPHICAL ABSTRACT



ARTICLE INFO

Article history:

Received 17 November 2018

Received in revised form 6 January 2019

Accepted 8 January 2019

Available online 14 January 2019

ABSTRACT

Combustion of fossil fuel is the dominant source of greenhouse gas emissions to the atmosphere in California. Here, we describe radiocarbon (¹⁴CO₂) measurements and atmospheric inverse modeling to estimate fossil fuel CO₂ (ffCO₂) emissions for 2009–2012 from a site in central California, and for June 2013–May 2014 from two sites in southern California. A priori predicted ffCO₂ mixing ratios are computed based on regional atmospheric transport model (WRF-STILT) footprints and an hourly ffCO₂ prior emission map (Vulcan 2.2). Regional

Abbreviations: ¹³CO₂, Carbon-13C dioxide; ¹⁴CO₂, Radiocarbon dioxide; CA, California; CARB, California Air Resources Board; CIT, California Institute of Technology; CEM, Cement production; COM, Commercial; CO₂, Carbon dioxide; EDGAR, Emission Database for Global Atmospheric Research; ffCO₂, Fossil fuel CO₂; GHGs, greenhouse gases; IND, Industrial; IPCC, Intergovernmental Panel on Climate Change; LSM, Land surface model; SCC South Central Coast, SDC San Diego County; MOB, On-road mobile; MYNN2, Mellor-Yamada Nakanishi Niino 2; NOAA, National Oceanic and Atmospheric Administration; SCC South Central Coast, SDC San Diego County; NOM, Non-road mobile; PBL, Planetary boundary layer; PG&E, Pacific Gas and Electric; PST, Pacific Standard Time; SBC, San Bernardino; SFBA, San Francisco bay area; SFBI, Scaling factor Bayesian inversion; SoCAB, South coast air basin; SJV the northern, San Joaquin Valley; SS Salton Sea, SSJV Southern San Joaquin Valley; STILT, Stochastic Time-Inverted Lagrangian Transport; SV, Sacramento Valley; UN, United Nations; US, United States; UTC, Coordinated Universal Time; UTL, Power production; RES, Residential; RMS, Root mean square; RMSE, Root mean square error; WRF, Weather Research and Forecasting; WGC, Walnut Grove; YSU, Yonsei University.

* Corresponding author at: 1 Cyclotron Rd, Berkeley, CA 94720, USA.

E-mail address: xcui@lbl.gov (X. Cui).

¹ Now at Bay Area Air Quality Management District, San Francisco, California, USA

Editor: Jianmin Chen

Keywords:

Atmospheric inversion
Tower-based measurements
ffCO₂ emissions
Seasonal variation
SFBA and SoCAB
Radicocarbon

inversions using observations from the central California site suggest that emissions from the San Francisco Bay Area (SFBA) are higher in winter and lower in summer. Taking all years together, the average of a total of fifteen 3-month inversions from 2009 to 2012 suggests ffCO₂ emissions from SFBA were within $6 \pm 35\%$ of the a priori estimate for that region, where posterior emission uncertainties are reported as 95% confidence intervals. Results for four 3-month inversions using measurements in Los Angeles South Coast Air Basin (SoCAB) during June 2013–May 2014 suggest that emissions in SoCAB are within $13 \pm 28\%$ of the a priori estimate for that region, with marginal detection of any seasonality. While emissions from the SFBA and SoCAB urban regions (containing ~50% of prior emissions from California) are constrained by the observations, emissions from the remaining regions are less constrained, suggesting that additional observations will be valuable to more accurately estimate total ffCO₂ emissions from California as a whole.

© 2019 Elsevier B.V. All rights reserved.

1. Introduction

Fossil fuel combustion is currently the main source of increasing atmospheric CO₂, driving changes in Earth's radiative balance, increasing surface temperatures and threatening the stability of the ecosystem services the Earth provides (IPCC, 2013). Global average CO₂ concentration has increased about 40% from the level of 278 ± 2 ppm in 1750 to over 400 ppm in recent years (Etheridge et al., 1996; NOAA, 2018). Emissions in urban regions contribute ~70% of the total global fossil fuel CO₂ (ffCO₂) emissions (UN, 2005). In California, ffCO₂ emissions in San Francisco Bay Area (SFBA) and South Coast Air Basin (SoCAB) are about half of the state's total ffCO₂ emissions (Gurney et al., 2009). In 2006, California enacted legislation designed to reduce greenhouse gas emissions (Legislative Information, 2006), so it is important to assess ffCO₂ emissions over time to verify those target reductions are occurring with more temporal and spatial observations.

Emission of ffCO₂, as well as other greenhouse gases (GHGs), can be estimated by both the 'bottom-up' and 'top-down' methods. The bottom-up inventories determine the fossil fuel emissions using data on fuel use, emitting activities, locations of power plants and spatial proxies (Gurney et al., 2009 and Gurney et al., 2012). However, bottom-up estimates may be limited by incomplete knowledge of processes that contribute to GHGs emissions. The 'top-down' method of atmospheric inversion uses bottom-up emissions estimates of GHGs in conjunction with atmospheric observations and meteorological Lagrangian transport models to estimate GHG emissions (e.g., Gerbig et al., 2003). Top-down methods have not yet been widely used for ffCO₂, however.

The State of California estimates emissions using bottom-up activity data including fuel sales and other data (CARB, 2016). As part of efforts to control emissions, it is valuable to independently evaluate the emission inventories using atmospheric measurements. Recent work has examined regional ffCO₂ emissions from California for short periods (e.g. Turnbull et al., 2011; Pataki et al., 2003; Newman et al., 2013; Brioude et al., 2013), and methods are being developed to monitor urban systems (Kort et al., 2013; Turnbull et al., 2015) as well as larger regions (Levin and Roedenbeck, 2008; Basu et al., 2016; Fischer et al., 2017; Graven et al., 2018). Graven et al., 2018 estimated ffCO₂ emissions across California using multiple towers, including the three we use here, for three one-month periods in 2014–15 and found that estimated emissions were consistent with those reported by the State of California. To our knowledge, there have not been estimates of ffCO₂ emissions over urban regions of SFBA and SoCAB using inversion modeling covering complete, continuous, annual timescales.

In this paper, we will describe atmospheric observation-based estimates of ffCO₂ emissions for SFBA and SoCAB, the two dominant major urban (and emitting) regions of California as shown in Fig. 1, which will make use of the four-year (2009–2012) tower-based observation data in SFBA and one-year data (2013–2014) to assess the annual and seasonal trend in SFBA and seasonal trend in SoCAB. In the methods section, we describe measurements of atmospheric ¹⁴CO₂ at three California sites, their use to estimate ffCO₂ enhancements, prediction of expected ffCO₂ enhancements using a priori emission maps and atmospheric transport

models, and estimation of posterior ffCO₂ emissions via Bayesian inversion. In the results, we report results for estimated ffCO₂ enhancements, and estimated annual and seasonal ffCO₂ emissions for SFBA and SoCAB. We then compare annual mean emissions with California's reported ffCO₂ emissions.

2. Methods

2.1. Air sampling and ¹⁴CO₂ measurements

Air was collected in flasks at one site in central California (WGC (Walnut Grove): 38.27°N, 121.49°W) and two sites in southern California (CIT (California Institute of Technology in Pasadena): 34.14°N, 118.12°W and SBC (San Bernardino): 34.09°N, 117.31°W) (see Fig. 1 for site locations and definition of the regions used for the inversions). Data from subsets of these sites have been used for previous regional estimates of methane (Jeong et al., 2012a, 2013, 2016, 2017) nitrous oxide (Jeong et al., 2012b; Jeong et al., 2018), and ffCO₂ emissions in California (Graven et al., 2018), and to investigate ffCO₂ in Southern California (Newman et al., 2013; 2016). In the current study, air sampling methods and analysis differed slightly among the different sites. For WGC, air samples were collected using automated flask packages as part of the NOAA Global Greenhouse Gas Reference Network (Andrews et al., 2014). Air was collected into flow-through flasks for approximately 2 min at 1400 PST (2200 UTC) approximately every 2–3 days from 91 m above the ground after passing through a water trap at 5 °C. At CIT, the air was collected on alternate days at ~10 m elevation above ground for approximately 1 min at 1400 PST into evacuated one-liter Pyrex flasks after passing through Mg(ClO₄)₂ to dry the samples. At SBC, air samples were collected at a height of 58 m above ground every three days from 1400 to 1500 PST in 1-h averages by varying the flow through 2-l flasks after passing through a water trap at 5 °C.

Air samples from WGC were sent to the NOAA Earth System Research Laboratory for measurement of total CO₂, δ¹³CO₂ and other stable greenhouse gases and reactive species not used in this study. CO₂ and δ¹³C were measured with precision at or better than 0.1 ppm and 0.01‰, respectively (Andrews et al., 2014). CO₂ samples collected by approximately 2–3 days were extracted and graphitized at the University of Colorado (Turnbull et al., 2006). Δ¹⁴C was analyzed by accelerator mass spectrometer at the Keck-CCMAS facility at the University of California, Irvine, using the methods described in Newman et al., 2013 and Xu et al., 2007. For the CIT and SBC samples, CO₂ was extracted from the air samples cryogenically, and analyzed following the methods described in Newman et al., 2008. Individual flask samples were analyzed for Δ¹⁴C weekly for SBC and bi-weekly for CIT by accelerator mass spectrometer at the Keck-CCMAS facility at the University of California, Irvine as well. Uncertainty in measured CO₂ concentrations at both CIT and SBC sites averages ± 1.4 ppm and $\delta^{13}\text{C} \pm 0.15\text{\textperthousand}$, where the large uncertainty in CO₂ is dominated by manometry with smaller contributions from extraction and mass spectrometry. Uncertainty for Δ¹⁴C is 2‰, based on the long-term reproducibility of secondary standards (Lehman et al., 2013; Newman et al., 2013).

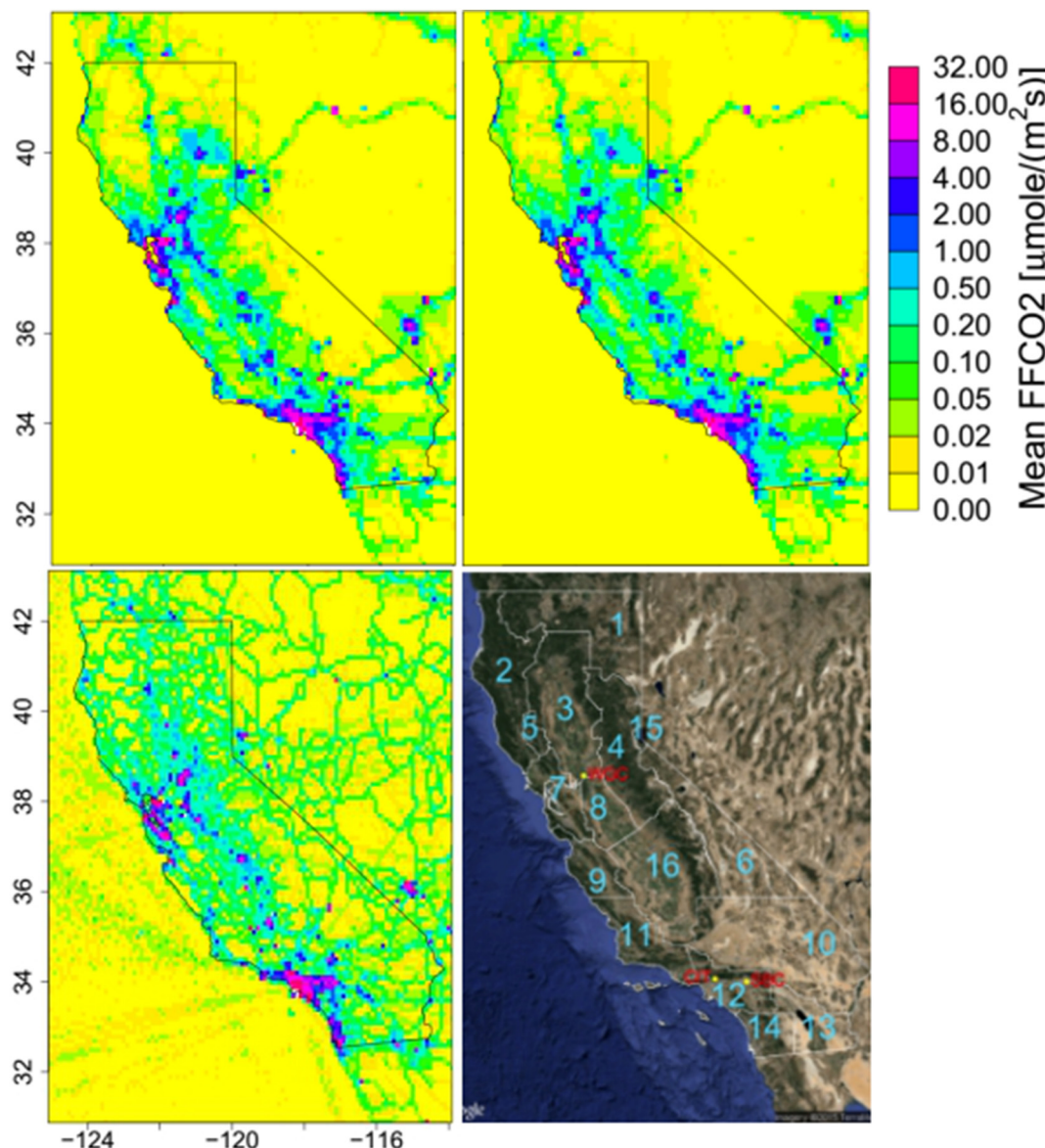


Fig. 1. Scaled prior fFCO₂ emissions from Vulcan V2.2 combined with EDGAR4.2 outside the US (top left); raw fFCO₂ emission map from Vulcan V2.2 combined with EDGAR4.2 outside the US (top right); raw fFCO₂ emission map of EDGAR4.2 (bottom left); region classification for fFCO₂ inversion (right). This region map is same as the Air Basin map (<https://www.arb.ca.gov/design/adm/basinnty.htm>) except that the San–Joaquin Valley was divided into two regions (Region 8 and Region 16). Regions 3, 7 and 8 are the Sacramento Valley (north Central Valley), San Francisco Bay Area, and the northern San Joaquin Valley (central Central Valley) in central California, and regions 10, 11, 12, 13, 14 and 16 are the Mojave Desert, South Central Coast, South Coast Air Basin, Salton Sea, San Diego County, and southern San Joaquin Valley air basins in southern California, respectively.

2.2. Estimation of atmospheric fossil fuel CO₂

Local enhancements (above background) of atmospheric CO₂ due to fossil fuel combustion were computed using a mass balance between local and background measurements of CO₂ using Δ¹⁴C (e.g., Miller et al., 2012; Turnbull et al., 2006) according to:

$$C_{obs} = C_{bg} + fFCO_2 + C_r - C_p \quad (1)$$

$$\Delta_{obs} C_{obs} = \Delta_{bg} C_{bg} + \Delta_{ff} fFCO_2 + \Delta_r C_r - \Delta_p C_p \quad (2)$$

where C is the mixing ratio of CO₂, Δ is the Δ¹⁴CO₂, obs is a local observation, bg is background, ff is fossil fuel component, p is net primary productivity and r is heterotrophic respiration, respectively. The impacts of air-sea fluxes, nuclear emissions and other types of biofuel

combustion such as wood on Δ¹⁴CO₂ are small as reported in Graven et al., 2018 and ignored as well in this study. Solving the above equation for fFCO₂, with the assumption that Δ_p = Δ_{bg} yields.

$$fFCO_2 = \frac{C_{obs} (\Delta_{obs} - \Delta_{bg})}{\Delta_{ff} - \Delta_{bg}} - \frac{C_r (\Delta_r - \Delta_{bg})}{\Delta_{ff} - \Delta_{bg}} \quad (3)$$

In the following work, we estimate C_{bg} and Δ_{bg} from smoothed records of Pt. Barrow, AK (Newman et al., 2016) since it has the data available in the study period. Measurements of Δ¹⁴CO₂ were similar to clean air sampled at La Jolla, CA in 1999–2007 (Graven et al., 2012; Newman et al., 2016) and the difference in calculated fFCO₂ at CIT using La Jolla or Barrow data was very small (~1%) (Newman et al., 2016). Raw radiocarbon data for WGC are compared to smoothed background results from

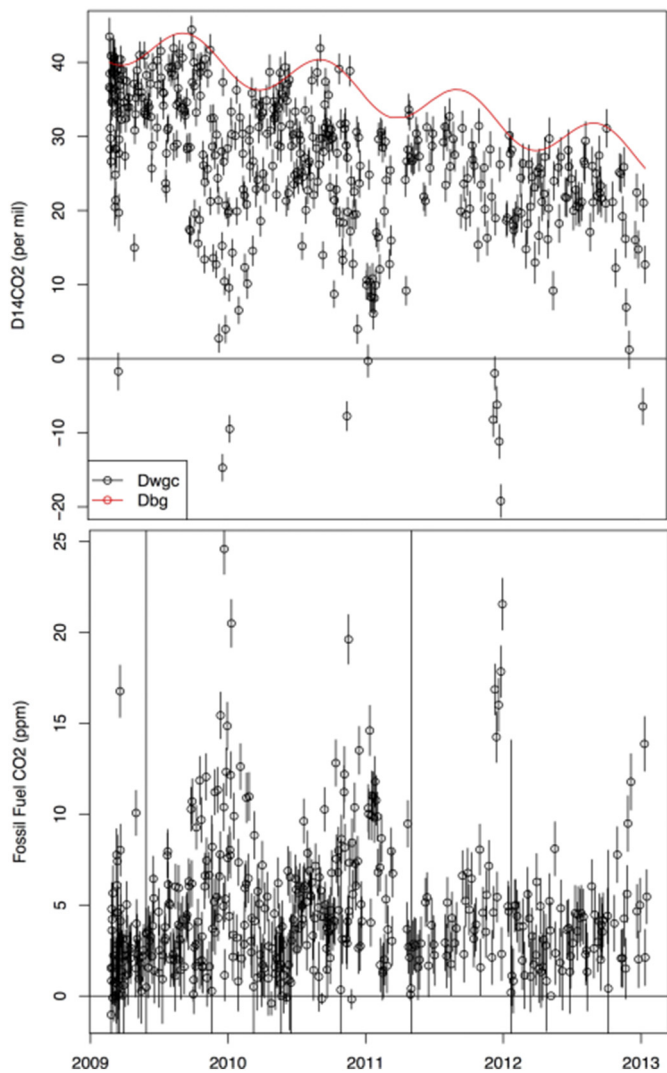


Fig. 2. Measured $\Delta^{14}\text{C}$ of CO_2 observed at WGC at 2009–2012 (DwgC in black) and the smoothed background (Dbg in red) obtained from Barrow, AK (top panel), and estimated fossil fuel CO_2 for WGC (bottom panel). The error bar means uncertainties of $\Delta^{14}\text{CO}_2$ and estimated fossil fuel CO_2 .

Pt. Barrow in Fig. 2 top. Δ_{ff} is -1000 per mil for fossil fuel because fossil fuels are assumed not to contain any ^{14}C due to decay of this short-lived radionuclide after millions of year (Newman et al., 2016). Because Δ_r is similar to Δ_{bg} as compared with Δ_{ff} , the 2nd term in Eq. (3) is assumed to follow a sinusoid with a small amplitude that varies with site following the approach described by Turnbull et al., 2006. We approximated the respiration term to vary from -0.2 ppm in winter to -0.5 ppm in summer for WGC (Turnbull et al., 2011; Fischer et al., 2017). Observations of $\Delta^{14}\text{C}$ and ff CO_2 at WGC are shown in Fig. 2 for the period from March 2009 – November 2012. ff CO_2 mixing ratios for WGC for the 2009–2012 study period are shown in Fig. 2 bottom. For CIT and SBC, where respiration is smaller and fossil fuel ^{14}C depletion of respired biomass CO_2 is likely greater, we used 0.06 in winter to 0.11 ppm in summer following Newman et al. (2016). For comparison with Graven et al., 2018, respiration corrections of magnitude 0.1 – 0.8 ppm at WGC and 0.0 – 0.5 ppm at CIT and SBC were calculated by simulating C_r using a biosphere model and atmospheric transport model, and using recent observations of Δ_r . While these more recent estimates are larger than our estimates of the respiration correction, the differences are small compared to the estimated ff CO_2 shown in Fig. 2.

2.3. Prior emission maps

A priori ff CO_2 emissions maps are prepared using the spatial and temporal distribution of the hourly Vulcan emission maps (version 2.2) developed for the 2002 emission year (Gurney et al., 2009; <http://vulcan.project.asu.edu/>). To estimate prior emissions for the years in this study, we scale the Vulcan emission maps by emission source sector to match in-state bottom-up ff CO_2 estimates provided by the California Air Resources Board (CARB) sector-specific greenhouse gas inventory for 2012 (CARB, 2014). The annual emissions for 2012 are 343 Tg CO_2/yr (CARB, 2014). For reference, the emissions for 2009–2012 are 341 , 337 , 329 and 336 Tg CO_2/yr , respectively, in a more recent version of the inventory (CARB, 2016), varying by $<4\%$. For the region outside the US (e.g., part of Mexico, Canada) where the Vulcan emissions are not available, the global Fast Track EDGAR 2010 emission inventory (EDGAR4.2, 2015) is used. The source sector definitions and the annual emissions from these sectors are listed in Table 1. The difference between the raw Vulcan and CARB 2012 (CARB, 2014) annual emissions for the cement production (CEM), industrial (IND), on-road mobile (MOB) and residential (RES) sectors is small relative to the CARB inventory ($<10\%$), while other sectors show larger variations up to a factor of 2.5 for aircraft (AIR), 70% for commercial (COM), 74% for non-road mobile (NON) and -29% for power production (UTL). Hence, the scaling of the original Vulcan emissions inventory to that of CARB leads to slightly different spatial distributions of ff CO_2 emissions for some sub-regions compared to the original Vulcan map. In order to retain variations in ff CO_2 emissions for weekdays relative to weekends we matched the weekday and weekend emission patterns of the CARB-scaled emission map to those of the original 2002 Vulcan data. The final annual average total emission map (summing from all source sectors) used for computing the predicted signals is shown in Fig. 1. ff CO_2 emissions are strongest in SoCAB and SFBA.

We use the combined CARB-scaled Vulcan and EDGAR (outside the Vulcan domain) emission map as our primary estimate of prior emissions but also use six other emission maps (Table S1) to evaluate the sensitivity of the inverse estimates to assumed prior emissions (Table 1). These include (1) the original (un-scaled) hourly-resolved Vulcan emission map within California and the EDGAR emission map out of the Vulcan domain, (2) the annual mean of the original (un-scaled) Vulcan emission and EDGAR map outside of the Vulcan domain, and (3) the EDGAR map alone (hereafter, original Vulcan, annual original Vulcan and EDGAR emission maps) (Fig. 1). The other three maps are (4 and 5) the scaled Vulcan map scaled by factors of 0.5 and 2, and (6) a flat prior map with a uniform flux of $1 \text{ umol/m}^2/\text{s}$ in each grid cell. The annual emissions in each region of California (see Fig. 1 for the regions) are listed in Table S1 for all prior maps used in this study. Here, prior emissions are 62 – 64 Tg CO_2/yr in SFBA (R07) and 105 – 128 Tg CO_2/yr in SoCAB (R12) across the different versions of Vulcan and EDGAR. As shown in Table S1, the emission differences are large between the flat prior map and the scaled Vulcan map, and those differences are used to define the prior emission uncertainty in the inversion. We note that the uncertainty of the flat flux prior emission varies among the 17 regions.

Table 1

Annual fossil fuel CO_2 emissions by sector for original and scaled Vulcan emissions and CARB 2012 inventory (unit = Tg CO_2/yr).

Source sectors	Vulcan V2.2 original	Vulcan V2.2 scaled	CARB GHG inventory
AIR (aircraft)	7.08	2.80	2.80
CEM (cement production)	6.38	6.89	6.89
COM (commercial)	24.18	14.13	14.12
IND (industrial)	68.36	75.88	75.87
MOB (on-road mobile)	145.55	152.22	152.19
NON (non-road mobile)	16.65	9.58	9.58
RES (residential)	28.26	27.81	27.74
UTL (power production)	38.24	53.73	53.74
State Total	335.7	343.0	342.9

2.4. Atmospheric transport modeling

The WRF-STILT (Weather Research and Forecasting and Stochastic Time-Inverted Lagrangian Transport) model (Lin et al., 2003; Skamarock et al., 2008; Nehrkorn et al., 2010) is used to simulate fFCO₂ concentrations. For the inter-annual analysis for WGC during March 2009–December 2012, we use the WRF simulations from Jeong et al., 2012a, 2012b, 2013. The WRF set-up for these simulations is summarized in Table S2 (for details see Jeong et al., 2012a, 2012b, 2013 and 2016; Bagley et al., 2017). For June 2013–May 2014, WRF3.5.1 is used to simulate meteorology for nested domains with 36, 12 and 4 km resolution (d01, d02, and d03) and two domains of 1.3 km resolution (d04 and d05) as shown in Fig. S1. The d03 domain (with 4 km horizontal resolution) covers most of California; d04 and d05 (with 1.3 km resolution) are used to represent the metropolitan area of Los Angeles and the San Francisco Bay Area, respectively. As with previous work, the WRF model was run with two-way nesting with 50 vertical levels to resolve meteorology over complex terrain features of California. Initial and boundary meteorological conditions are driven by the North American Regional Reanalysis data set (Mesinger et al., 2006). Based on the transport evaluation using measured and predicted CO mixing ratios (Bagley et al., 2017), we apply the Mellor–Yamada Nakanishi Niino 2 (MYNN2) scheme to model planetary boundary layer (PBL) for all the months for the CIT site. For the SBC site, the Yonsei University (YSU) scheme is used for November–January while MYNN2 is used for the other months since YSU boundary layer scheme enables a WRF parameterization designed to improve the representation of topographic effects (Bagley et al., 2017). For the land surface model (LSM), the Noah LSM is used for all seasons at both CIT and SBC (Newman et al., 2013). WRF simulations are conducted for each day separately, starting 6 h before the day of simulation to provide model spin-up (Jeong et al., 2012a, 2012b, 2013; Bagley et al., 2017).

Particle trajectories for each simulated receptor location and time point are estimated from the hourly WRF output by releasing an ensemble of 500 STILT particles at heights corresponding to the sampling locations: 91 m above ground (WGC), 10 m (CIT), and 58 m (SBC). The particles are run backward for 7 days driven by the WRF output within the smallest domain grid available for that location (i.e., d03, d02, d01 for WGC; and d04, d03, d02 and d01 for CIT and SBC). Footprints are computed by aggregation of particles weighted by the time spent at a given location and the inverse of the planetary boundary layer depth at that location. Fig. S2 shows mean footprints for the flask receptors at sites of WGC (Jeong et al., 2012a, 2012b and 2013), CIT and SBC, which are computed from the best schemes in Bagley et al., 2017. Generally, footprint sensitivity is largest near the receptor sites and tracks the upwind direction backward in time. There are clear seasonal patterns for the distribution of footprints at the measured sites as seen in Fig. S2. As in Jeong et al., 2012a, 2012b, 2013, 2016, 2017 and 2018, we only use an observation in the inversion when the majority of the particles (80%) for that observation reach the western boundary of the modeling domain at 130°W.

2.5. Bayesian inverse model

2.5.1. Inversion approach

We use the scaling factor Bayesian inversion (SFBI) method used in previous studies (e.g., Jeong et al., 2012a, 2012b, 2013; Fischer et al., 2017), which relates model predictions to observations as,

$c = K\lambda + v$ (4) where c is the observed background-subtracted mixing ratio. In this study, it represents the reconstructed fFCO₂ that is calculated from Eq. (3). K is the predicted mixing ratio computed from the footprint, F , and prior emissions, E , as $K = FE$. Here, λ is a set of scaling factors to scale prior emissions, and v is the model-data mismatch vector with covariance matrix R . R is a diagonal matrix representing the total uncertainty summed in quadrature by all error sources such

as the measurement error and the transport error. Under Gaussian assumptions, the posterior estimate for λ is solved as

$$\lambda_{post} = \left(K^T R^{-1} K + Q_\lambda^{-1} \right)^{-1} \left(K^T R^{-1} c + Q_\lambda^{-1} \lambda_{prior} \right) \quad (5)$$

where λ_{prior} is the a priori estimate for λ , and Q_λ is the error covariance associated with λ_{prior} . The posterior error covariance for λ can be given as,

$$V_{post} = \left(K^T R^{-1} K + Q_\lambda^{-1} \right)^{-1} \quad (6)$$

The SFBI method is used to estimate optimal emissions at both seasonal and annual temporal scales for the WGC site (central California) and the combined CIT and SBC sites (southern California) and negative mixing ratios are not included in the inversion modeling. The inverse modeling is implemented in two steps (first and final) as in Bergamaschi et al., 2005, and Jeong et al., 2012a, 2012b, 2013. After the first inversion, the second/final inversion is conducted using data selected by another set of criteria, $|c_i - (K\lambda)|^2 < \alpha R_i$ where α is a factor applied to error covariance matrix R_i . The values of α are determined to optimize the chi-square statistics to ~1 (α range from 2 to 3). This process is similar to that of McKain et al., 2015 who excluded data points with model-data residuals $>3\sigma$ from the emission calculations.

Following previous work using the same inversion setup (Jeong et al., 2016; Fischer et al., 2017), we estimate 17 scaling factors (i.e., 16 regions in California and one region outside California), representing the regions shown in Fig. 1 (bottom right). Here, the regions used for the inversions are constructed following a map of 15 “air basins” classified by CARB for air quality control (<https://www.arb.ca.gov/desig/adm/basincnty.htm>), with a further subdivision of the San Joaquin Valley into northern (Region 8) and southern (Region 16) regions. We use the inversion setup previously established by Jeong et al., 2016 and Fischer et al., 2017, even though the limited number of sites we have for fFCO₂ here is not sufficient to provide observational constraints for all 16 regions in California. However, it was more convenient to use this existing setup than to modify the inversion setup. In the following analysis, we focus on emissions in central and southern California regions, particularly from SFBA (Region 7) and SoCAB (Region 12), because our observation sites are located in or near these regions and significant reductions in posterior uncertainties are found in the regions. We aggregate WGC observations into 15 individual 3-month (season) periods, 4 average “seasons” (combining same seasons from 2009 to 2012 together), and 4 years (combining data for each year together). For southern California, we estimate seasonal emissions (3-month averages) for the June 2013–May 2014 period using the CIT observations alone, the SBC observations alone, and both CIT and SBC combined, respectively.

2.5.2. Uncertainty estimates

In SFBI, the error covariance matrix, R , represents the expected model-measurement mismatch error for each observation. Here, R is expressed as a diagonal matrix assuming uncorrelated errors, where each element represents the total uncertainty (as a quadrature sum) from different error sources including the number of particles released, flux aggregation, errors in modeled atmospheric transport, estimated background mixing ratios (Gerbig et al., 2003; Zhao et al., 2009; Göckede et al., 2010; Jeong et al., 2013) and the error from the observation.

Following Fischer et al., 2017, we estimated the R matrix as a quadrature sum of two components: 1) the mean measurement error in estimated fFCO₂, and 2) a term proportional to the mean observed fFCO₂ signal from Eq. (3) at each site since it is very complex to compute the R matrix explicitly from all sources, and the second term, which presents all of the model-related error sources aforementioned, tends to be dominated by atmospheric transport model error with a magnitude that is generally about half of the background-subtracted atmospheric

signals as shown in (Jeong et al., 2012a, 2012b, 2013). Here, each component of \mathbf{R} is calculated as

$$\mathbf{R}_i = \text{mean}(\text{ffCO}_2 \text{ observation error})^2 + (\text{frac}^* \text{mean}(\text{ffCO}_2 \text{ observation}))^2 \quad (7)$$

where frac is the fraction to scale the mean seasonal reconstructed ffCO_2 , which is a ratio presenting how much the mean observed ffCO_2 is considered in the R matrix. The average observed ffCO_2 for each season is shown in Table 2 for different sites. To examine the sensitivity of posterior emission estimates to the assumed model-data mismatch uncertainty, three different values of 0.3, 0.5 and 0.7 are used for frac . For example, with a factor of 0.5, we prescribe 50% of the mean ffCO_2 . In the results, we focus on the result using the assumed factor of 0.5 and discuss the sensitivity test results depending on the assumption on the fractional error. We note this is a reasonable assumption because Bagley et al., 2017 found that the annual fractional RMSE (root-mean-square error) of predicted CO versus observed CO for CIT, SBC, and WGC site were 0.35, 0.46 and 0.51, respectively, using similar meteorological simulations. Moreover, the median fractional RMSE estimated from the hierarchical Bayesian inversion (Graven et al., 2018) for CIT, SBC, and WGC ranged from 0.4 to 0.7, similar to the range we use. In this work, we use 1.4 ppm for ffCO_2 observation error for all months at the CIT and SBC sites based on the estimated measurement errors described above, and <1.68 ppm for WGC depending on season.

Under the assumption that uncertainties in prior emissions are uncorrelated between different regions, the prior model uncertainty is expressed in the diagonal matrix \mathbf{Q} . For this work, we assume that the uncertainty in the ffCO_2 emissions at the air basin level is estimated at 25% ($1-\sigma$), based on a county level comparison of Vulcan emissions with an independent California-specific bottom-up fuel use estimates for counties in California (de la Rue du Can and Price, 2008). Under the assumption that the uncertainties between regions are uncorrelated, summing 25% emission uncertainties at the regional scale in quadrature yields a ~10% ($1-\sigma$) uncertainty in state-total ffCO_2 emissions, similar to earlier assessments of likely uncertainty in annual ffCO_2 emissions for countries with detailed accounting standards (National Research Council, 2010), and a recent comparison of multiple ffCO_2 emission models reported by Fischer et al., 2017. The estimated multi-model uncertainty of ffCO_2 prior emissions for SFBA obtained in a previous study by Fischer et al., 2017 was 23%, though the result for SoCAB was 10%. We calculated the uncertainty in annual emissions by averaging the uncertainty from each 3-month inversion. Here, we average the diagonal component of posterior uncertainty corresponding to each region (e.g., SFBA or SoCAB) which include the effect of uncertainties correlated with those from other regions (Jeong et al., 2013). The t -test was applied to check whether the estimated emissions are significantly different between summer and winter by using Welch's t -test (Welch, 1947). If p value is <0.05, it is significantly different, otherwise not. Here, we emphasize that measurement and model input uncertainties are reported as 1-sigma (68% confidence) intervals, while

posterior emission estimates are reported as 2-sigma (95% confidence) intervals.

3. Results

3.1. ffCO_2 mixing ratios

The ffCO_2 mixing ratios at WGC are shown in Fig. 3 (top) for the period from March 2009–November 2012. Both the predicted (from the scaled Vulcan map) and observed ffCO_2 vary with season in Fig. 3, showing the largest ffCO_2 in winter, consistent with the observed seasonality of boundary layer depth in California (Bianco et al., 2011). We acknowledge background, respiration, and difference in actual ffCO_2 emissions are possible explanations for the variation as well. The average observed ffCO_2 is larger than 6.5 ppm in all winters, while the ffCO_2 in other seasons averages 3–6 ppm, as shown in Table 2. For southern California, we make use of the measurements at CIT and SBC during the period of June 2013–May 2014. Here, time averages of predicted daily ffCO_2 from the scaled hourly Vulcan map are computed to match the aggregation of air samples as described in Section 2.1. As shown in Fig. 3, the measured and predicted ffCO_2 at CIT are much larger than those at SBC.

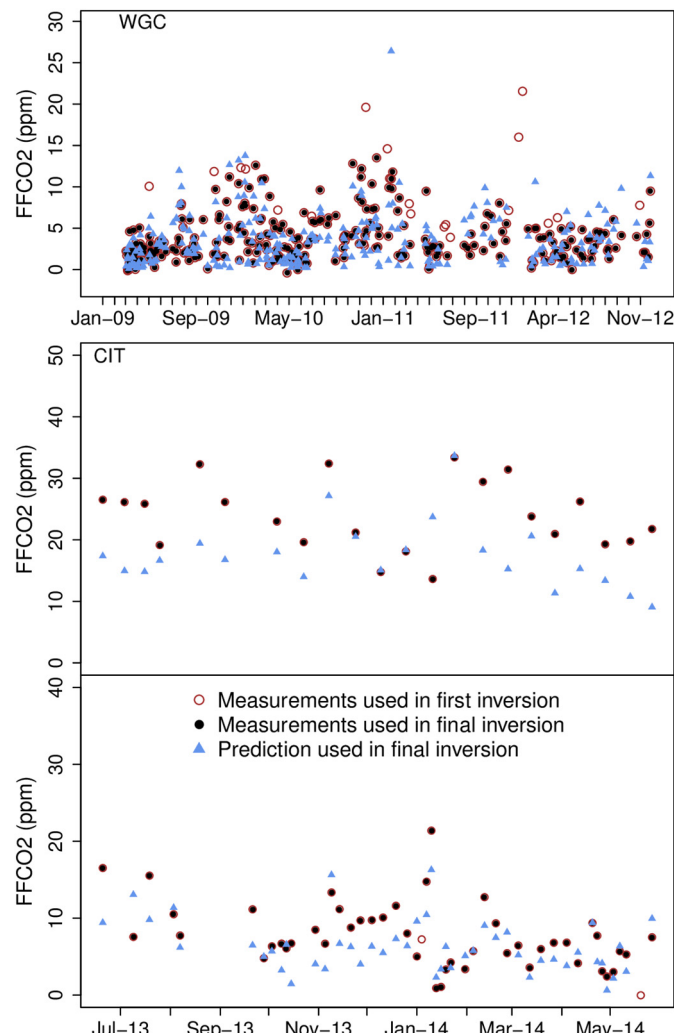


Fig. 3. ffCO_2 at WGC (top), CIT (middle) and SBC (bottom). Observed ffCO_2 used in the first inversion (gray open circle), observed ffCO_2 mixing ratio used in the final inversion (black filled circle), and WRF-STILT predicted ffCO_2 mixing ratios from scaled Vulcan map (used in final inversion). The temporal label is month-year.

Table 2

Mean reconstructed ffCO_2 observed at WGC during 2009–2012 and at CIT and SBC during 2013–2014 (unit = ppm).

Site	Year	Winter	Spring	Summer	Fall
WGC	2009	NA	3.0	3.5	5.1
WGC	2010	8.0	2.9	4.5	5.8
WGC	2011	7.1	3.4	3.3	4.9
WGC	2012	6.6	3.1	3.4	4.1
CIT	2013–2014	25.0	21.6	25.9	21.5
SBC	2013–2014	8.2	5.1	11.0	10.2

3.2. ffCO₂ emissions in central California

3.2.1. Bayesian estimates of ffCO₂ emissions in central CA

Results for Bayesian inversions for 15 seasons (omitting 2009 winter due to the small amount of data) are presented in Table 3. As described above, outliers are identified and removed after the first inversion. For most seasons, no more than two data points are removed, with an exception of summer 2011 where three data points are removed. The average number of data points in the final inversion is 21.

Table 3 provides a summary of best-fit regression slopes and RMS errors for predicted vs. observed ffCO₂ in different seasons before and after the inversions. The optimization generally reduces the RMS error of (predicted vs. measured) ffCO₂ and adjusts the best-fit slope toward unity. For instance, in spring 2012 the best-fit slope is improved from 1.48 ± 0.65 (RMS error = 3.28 ppm) to 1.39 ± 0.29 (2.00 ppm), where uncertainties in slope are reported at 1-sigma. However, both the posterior regression slopes are roughly consistent with unity, suggesting consistency between predicted and measured ffCO₂ signals.

The annual average posterior ffCO₂ emissions for 2009–2012 are shown in Fig. 4, calculated by averaging the four seasonal emission estimates in each year (with 2009 missing winter as described above). Averaging posterior emissions over the 2009–2012 period, posterior emissions (60 Tg CO₂/yr) are consistent with the prior (64 Tg CO₂/yr) but uncertainty in the prior of 32 Tg CO₂/yr is reduced to 22 Tg CO₂/yr, or roughly 50% uncertainty is reduced to 34% (where both are expressed at 2-sigma or 95% confidence) for the SFBA, suggesting the WGC observations provide a constraint on SFBA emissions. Much smaller uncertainty reductions are obtained for the Sacramento and North San Joaquin Valley regions (12 Tg CO₂/yr is reduced to 10 Tg CO₂/yr and 6 to 5 Tg CO₂/yr), and henceforth we focus on the SFBA. The posterior error covariance coefficients for SFBA, Sacramento and North San Joaquin Valley regions are <5%, indicating that posterior SFBA emissions weakly co-vary with those of other regions (Tarantola, 1987; Jeong et al., 2012a).

Emissions in SFBA vary seasonally with emissions of 61 ± 21 , 48 ± 16 , 62 ± 23 and 69 ± 29 Tg CO₂/yr (all at 95% confidence) in spring, summer, fall, and winter, respectively, as shown in Fig. 5. The higher emission in winter relative to summer is significant (applying Welch's *t*-test (Welch, 1947), *p* < 0.05). We note the seasonal variation in posterior emissions is larger than that estimated in Vulcan 2.2, where SFBA emissions vary as 63, 59, 61 and 67 Tg CO₂/yr in spring, summer, fall, and winter, respectively. This suggests that the observations provide additional information not contained in the prior emission map. Also, the variation of Vulcan prior map emission is mainly due to varied emission in residential usage, which is highest in winter and lowest in summer. The standard deviation of seasonal emissions of residential usage is as large as 3.8 Tg CO₂/yr, but they are <1 Tg CO₂/yr for other emission sectors. Examining inter-annual variation, posterior emissions from SFBA are 57 ± 20 , 70 ± 22 , 62 ± 23 , and 51 ± 23 Tg CO₂/yr for 2009 to 2012 (all at 95% confidence), respectively. The results do not show significant inter-annual variation in emissions (*p* > 0.05), nor any significant trend over the 2009–2012 period.

Table 3

Best-fit slopes from regression of predicted ffCO₂ from scaled Vulcan map vs. observed ffCO₂ at WGC (at 1-sigma, 68% confidence) before and after inversion during 2009–2012 (prior uncertainty = 0.25, frac = 0.5 and ocean cut used).^a

Year		Winter	Spring	Summer	Fall
2009	Before inversion	NA	0.82 ± 0.22 (1.91 ppm)	1.36 ± 0.4 (2.86 ppm)	0.92 ± 0.14 (2.92 ppm)
	After final inversion	NA	0.89 ± 0.20 (1.38 ppm)	0.83 ± 0.26 (1.90 ppm)	1.10 ± 0.12 (2.09 ppm)
2010	Before inversion	1.02 ± 0.22 (3.53 ppm)	0.57 ± 0.11 (1.99 ppm)	0.81 ± 0.14 (2.22 ppm)	0.62 ± 0.15 (4.01 ppm)
	After final inversion	1.06 ± 0.22 (2.89 ppm)	0.71 ± 0.12 (1.66 ppm)	0.93 ± 0.11 (1.46 ppm)	0.92 ± 0.08 (1.77 ppm)
2011	Before inversion	1.32 ± 0.43 (5.36 ppm)	0.63 ± 0.23 (2.6 ppm)	-1.86 ± -2.77 (3.05 ppm)	1.49 ± 0.85 (2.92 ppm)
	After final inversion	1.04 ± 0.22 (3.74 ppm)	0.84 ± 0.23 (1.85 ppm)	1.53 ± 0.74 (1.32 ppm)	1.35 ± 0.51 (2.33 ppm)
2012	Before inversion	0.42 ± 0.46 (6.91 ppm)	2.90 ± 1.06 (4.59 ppm)	1.54 ± 0.67 (2.07 ppm)	1.48 ± 0.65 (3.28 ppm)
	After final inversion	1.42 ± 0.47 (2.12 ppm)	1.00 ± 0.49 (1.63 ppm)	1.15 ± 0.54 (1.63 ppm)	1.39 ± 0.29 (2.00 ppm)

^a The values in the parentheses are RMS errors.

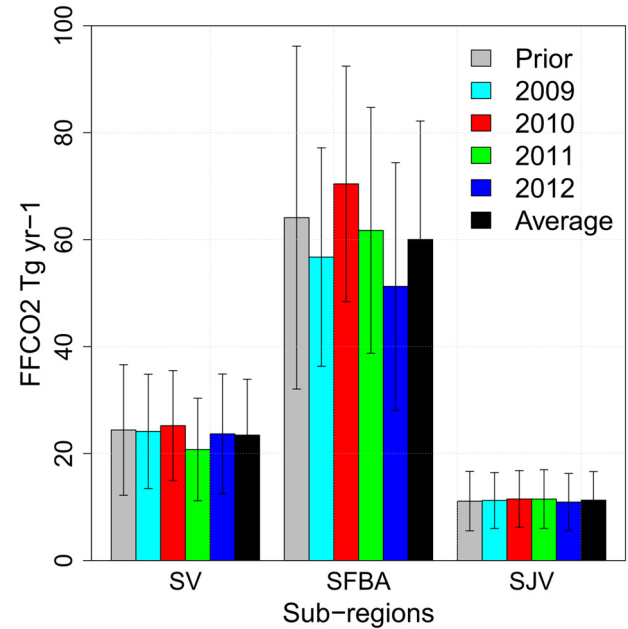


Fig. 4. Annual average prior and posterior ffCO₂ emissions from scaled Vulcan map (error bars show prior and posterior uncertainties at 95% confidence) based on 15 seasonal inversions in central California using measurements from WGC tower (factor for R matrix = 0.5; ocean cut used). SV, SFBA and SJV represent the Sacramento Valley (north Central Valley), San Francisco Bay Area, and the northern San Joaquin Valley (central Central Valley), each of which corresponds to Regions 3, 7 and 8, respectively (see Fig. 1).

The results for the SFBA suggest that the observations provide variable constraint on posterior emissions, with a maximum influence in summer and a minimum in winter. Following Turner et al., 2015, we estimate the fractional constraint on posterior emissions provided by the observations relative to the constraint imposed by the prior in the seasonal average diagonal elements of the averaging kernel matrix (calculated as $\mathbf{I} - \mathbf{V}_{\text{post}} \mathbf{Q}^{-1}$ where \mathbf{I} is the identity matrix). Here, a value of unity suggests the observations constrain the emissions fully while the value of zero indicates no constraint. The corresponding values for SFBA from the seasonal averaging kernel matrix are 0.58, 0.72, 0.45, 0.28 for spring, summer, fall, and winter, respectively, suggesting maximum constraint of 72% in summer and minimum constraint of 28% in winter. This variation is qualitatively consistent with the footprint analysis in this study and previous inversion results by Jeong et al., 2012a, 2012b, 2013, 2016 and 2017 where the summer footprints of WGC are strongest from SFBA to the west of WGC constraining SFBA emissions. During winter, WGC footprints are strongest in the Central Valley, more weakly constraining SFBA.

3.2.2. Sensitivity tests

We compare average posterior emissions for SFBA using the original Vulcan, annual average Vulcan, and EDGAR emission maps to examine

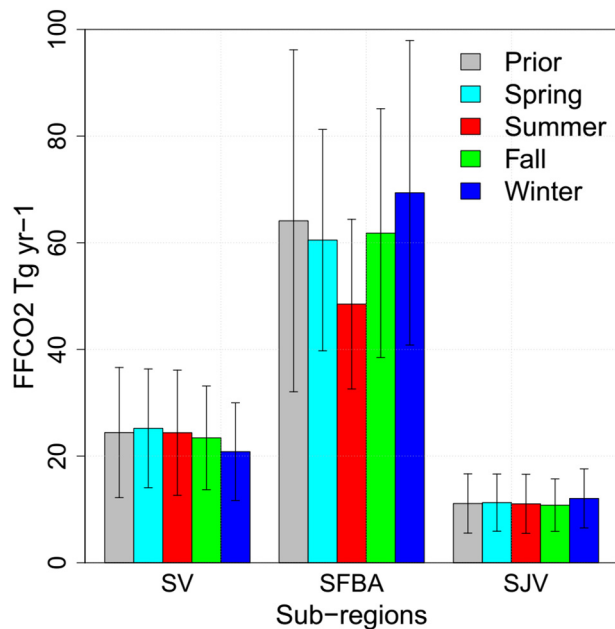


Fig. 5. Seasonal average posterior ffCO₂ emissions from scaled Vulcan map (posterior uncertainty at 95% confidence) based on 15 seasonal inversions in central California using measurements from WGC tower (factor for R matrix = 0.5; ocean cut used). SV, SFBA and SJV represent the Sacramento Valley (north Central Valley), San Francisco Bay Area, and the northern San Joaquin Valley (central Central Valley) and they are Regions 3, 7 and 8 in Fig. 1 (bottom right).

the impact of prior emissions on the inversion result. As shown in Table 4, in each case, posterior emissions are indistinguishable from the estimate of 60 ± 22 Tg CO₂/yr (95% confidence) obtained with the scaled Vulcan map. This means that scaling the Vulcan map doesn't impact estimating the posterior emission in SFBA significantly.

Next, we assess the ability of the observations to correctly recover regional emissions when starting with false prior emissions, either multiplying the Vulcan map by 50% and 200% or starting with the flat prior map (Table 4). By design, the prior emissions from these false prior maps (32, 128 and 24.3 Tg CO₂/yr in SFBA) are quite different from the scaled Vulcan emissions (64 Tg CO₂/yr) and this test determines whether posterior emissions based on deliberately biased prior emissions are consistent with the posterior emissions based on the scaled Vulcan prior emission, within uncertainties. The posterior emissions obtained with the false prior maps are 40 ± 14 , 70 ± 30 and 34 ± 56 Tg CO₂/yr (all at 95% confidence) for the 50% and 200% scaled Vulcan map and the flat prior map (Table 4), which are all consistent with the posterior obtained with the scaled Vulcan prior emissions (60 ± 22 Tg CO₂/yr at 95% confidence). This suggests that the inversion system driven by the radiocarbon observations does provide some constraint on ffCO₂ emissions in SFBA. For the flat prior map, the posterior

uncertainty is very large, showing that it is necessary to use a prior map with realistic spatial distribution of emissions. This can be expected since ffCO₂ emissions vary substantially over the SFBA region (Fig. 1) and the WGC site may be sensitive to only part of the SFBA region.

Next, we examine the effect of varying the model-data mismatch uncertainty across three different factors ($\text{frac} = 0.3, 0.5$, and 0.7). We also analyze the sensitivity of inversion to background data filtering where we remove data for observations when <80% of the particle trajectories reach the western edge of the model domain at 130°W (referred to as "ocean cut"). The reasoning behind this filtering is that the background values we have used may be unsuitable for air masses entering California from directions other than from the west. The posterior emissions based on different inversion set-ups are summarized in Table S3, with ratios between posterior and prior emissions in SFBA ranging from 0.76 ± 0.16 to 0.94 ± 0.35 (all at 95% confidence). The implementation of background data filtering tends to increase the posterior emissions (so they are more similar to the prior) and increase the posterior uncertainties, compared to excluding the background data filtering, likely because of the weaker data constraint from fewer observations in the inversion. As the posterior estimates from these tests are all similar, it appears that the posterior emissions are only weakly sensitive to the assumed model-measurement uncertainty and the inclusion of background data filtering.

Last, we test the sensitivity of the inversion to the assumption on the prior uncertainty by using prior uncertainties ranging from 12.5% to 75% (as 1-sigma, equivalent to 35% to 150% at 95% confidence). Here, results for SFBA show that while posterior emissions vary with the assumed prior uncertainty (Table S4), they remain statistically indistinguishable ($p > 0.05$). This is because the mean changes by only 7% (58–62 Tg CO₂/yr) while the posterior uncertainties are 23% or more, and proportional to the prior uncertainty. The increase of the posterior uncertainty with an increase in the prior uncertainty is typical in this type of inversion (Jeong et al., 2012a; Wecht et al., 2014), but the small changes in the central estimate of the posterior emissions suggests that it is not substantially affected by the assumed prior uncertainty. In addition, the posterior emission is 50 ± 22 Tg CO₂/yr at 95% confidence from the 50% scaled Vulcan map with the prior uncertainty of 50%, which is much closer to the 'best estimated' emission of 60 ± 22 Tg CO₂/yr at 95% confidence than the inversion estimation from scaled hourly Vulcan map and 25% uncertainty. This further supports the reliability of the tests of sensitivity of the estimated emissions to the prior uncertainty are reliable suggesting our observations constrain the regional total emission for SFBA.

Taken together, the sensitivity tests described above demonstrate that the inverse estimates of ffCO₂ emissions for the SFBA region are resilient to the choice of prior emission map (false maps, Vulcan maps and EDGAR maps), and prior emission and measurement-model uncertainties.

3.3. ffCO₂ emissions in southern California

3.3.1. Bayesian estimates of ffCO₂ emissions in southern CA

Applying the standard inversion with the scaled hourly Vulcan prior emissions (prior uncertainty = 25%, and $\text{frac} = 0.5$), the posterior emissions for seasonal inversions for southern California sub-regions are shown in Fig. 6. Here, the measurements from CIT and SBC reduce posterior uncertainty in SoCAB (region 12), with only minor uncertainty reductions in other regions, and so we focus on SoCAB. For SoCAB annual average posterior emissions are 124 ± 31 Tg CO₂/yr, consistent with the prior value of 109 ± 54 Tg CO₂/yr (where both are expressed at 95% confidence), but with a reduction of uncertainty. For comparison, inversions using only CIT or SBC data produce results that are similar to those above, with annual average posterior emissions of 124 ± 42 and 113 ± 35 Tg CO₂/yr (all at 95% confidence) using either CIT or SBC, respectively.

Examining seasonality with all observations from CIT and SBC, the posterior emissions are 118 ± 28 , 132 ± 37 , 114 ± 31 , 131 ± 27 Tg

Table 4

Prior and posterior ffCO₂ emissions in units of Tg CO₂/yr for the San Francisco Bay Area (uncertainty at 95% confidence) from all prior maps listed in first column based on 15 seasonal inversions for central California (prior uncertainty = 0.25, factor for the R matrix = 0.5 and ocean cut used).

Prior maps	Prior emissions	Posterior emissions (unit = Tg CO ₂ /yr)
Scaled Vulcan map	64 ± 32	60 ± 22
Original Vulcan map	62 ± 31	62 ± 23
Annual original Vulcan map	62 ± 31	61 ± 23
EDGAR map	64 ± 32	65 ± 25
50% scaled Vulcan map	32 ± 16	40 ± 14
200% Scaled Vulcan map	128 ± 64	70 ± 30
Flat Flux map	24 ± 12	34 ± 56

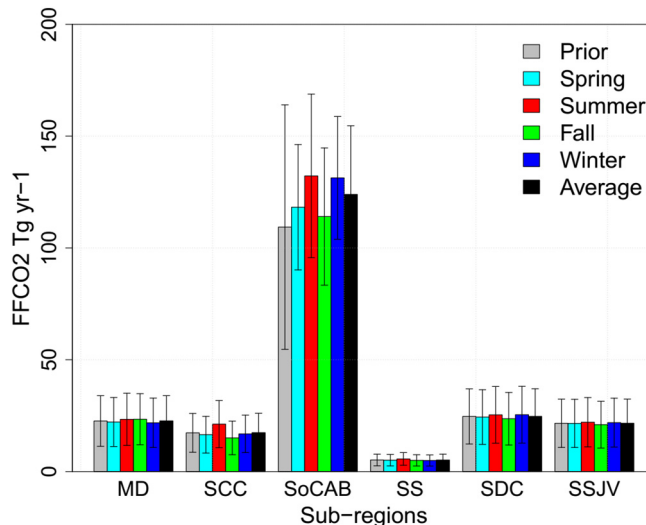


Fig. 6. Seasonal posterior fFCO₂ emissions from scaled Vulcan map (posterior uncertainty at 95% confidence) in regions of southern California using combined measurements from CIT and SBC towers (factor for the R matrix = 0.5; ocean flag used). MD, SCC, SoCAB, SS, SDC and SSJV represent the Mojave Desert, South Central Coast, South Coast Air Basin, Salton Sea, San Diego County, and southern San Joaquin Valley air basins, respectively and they are Regions 10, 11, 12, 13, 14 and 16 in Fig. 2 (right).

CO₂/yr (all at 95% confidence) for spring, summer, fall, and winter, respectively, with slightly higher emissions in summer and winter when more electricity is used for air conditioning and heating, though the effects are not statistically significant ($p > 0.05$). These are consistent with the Vulcan 2.2 prior map that the emission variation is contributed by sectors of the transportation, residential usage and power production with standard deviation of 3, 5 and 3 Tg CO₂/yr in comparison with other sectors <1 Tg CO₂/yr. The higher emissions in the winter are mainly contributed by the residential usage, and the higher emissions in summer are due to mobile on-road and power production sectors.

Here, the emissions for SoCAB (Region 12) show normalized covariance of -0.03 with Region 13, which suggests only a weak correlation between the two adjacent regions and further indicates the SoCAB emissions have been estimated independently. As above, we also estimate the diagonal elements of the averaging kernel matrix following Turner et al. (2015), finding values for SoCAB of 0.72, 0.58, 0.64 and 0.77 for spring, summer, fall and winter, respectively. This result indicates that overall, the emissions in SoCAB are constrained by the observations somewhat better than in SFBA, likely due to the fact that observations from two sites are used to constrain SoCAB emissions and because the fFCO₂ signals are larger.

3.3.2. Sensitivity tests

Applying the tests with false prior maps in SoCAB (w/ prior emissions of 55, 218 and 32 Tg CO₂/yr), posterior emissions are 81 ± 22 , 130 ± 36 and 79 ± 82 Tg CO₂/yr (all at 95% confidence) are statistically indistinguishable for the 50% and 200% Vulcan emission maps, and the flat flux prior map, respectively. These results are also consistent with the result obtained with the scaled hourly Vulcan prior emission, suggesting that the observations and modeling system are effective in estimating posterior emissions (albeit with greater uncertainty) despite a substantially incorrect prior assumption.

The sensitivity tests on the model-measurement uncertainty, time averaging of the prior, and removal of data for the case when particle trajectories do not reach the western edge of the model domain are summarized in Table S5. Here, the scaling factors (ratio of posterior to prior) range from 1.06 ± 0.17 to 1.19 ± 0.11 at 95% confidence depending on the assumptions. With the exception of a very small model-measurement uncertainty (frac = 0.3), the variations in posterior emissions are small. In addition, when the scaled Vulcan prior emissions are

replaced with the original Vulcan, annual original Vulcan and EDGAR emission maps, the posterior emissions change by < 3 Tg CO₂/yr, compared to the posterior uncertainties of 30 Tg CO₂/yr (Table 5).

The results show weak sensitivity to the choice of prior uncertainty (posterior/prior factor shown in Table S4) and statistically indistinguishable posterior emissions among different assumptions, suggesting that the inversions are only weakly sensitive to the prior uncertainties. In addition, the estimated emission using scaled Vulcan map by 50% with 50% 1-sigma prior uncertainty assumption is 107 ± 30 Tg CO₂/yr at 95% confidence, which is consistent with the estimate of 124 ± 31 Tg CO₂/yr at 95% confidence from scaled Vulcan map with 25% 1-sigma prior uncertainty. This results further support that the inversion result is not strongly influenced by our choice of prior uncertainty.

As with the results for central California, these sensitivity tests demonstrate that the SoCAB measurements provide constraint on posterior fFCO₂ emissions that are consistent across a range of prior emission maps (false maps, Vulcan maps and EDGAR map), different inversion setting ups (different ways of combining data, different fraction values for R etc.) and different prior uncertainties (seeing Table 5). Furthermore, scaling the Vulcan map doesn't impact the estimation of emissions in SoCAB significantly as shown in Table 5.

4. Discussion

The estimated total emissions for SFBA averaged over the 2009–2012 period is 60 ± 22 Tg CO₂/yr at 95% confidence, which is $94 \pm 35\%$ of prior emissions for the region. Our inter-annual analysis for SFBA (see Fig. 4) does not detect a significant inter-annual variation or trend in emissions. However, the seasonal variation in posterior emissions is statistically significant with emissions larger in winter than summer, consistent with variations in natural gas consumption in the SFBA (PG&E, 2016). Although the Vulcan 2.2 prior map shows the seasonal variation is mainly contributed by the residential usage, source inversion will be helpful for the source-attribution study of fFCO₂ emission in the future with additional tracer such as CH₄.

Comparing with other studies, the estimated annual emissions in SFBA (and SoCAB) are consistent with the shorter term estimates obtained in Graven et al., 2018. However, the uncertainty reduction obtained in this work ($1-\sigma$ posterior uncertainty/prior uncertainty) is smaller than that predicted by Fischer et al., 2017 (Table 4) or obtained by Graven et al., 2018 (Fig. 3). This may be due to those studies using more measurement sites than the three tower sites used in this study (Brophy et al., 2018). Thus, it is necessary to adopt measurements from multiple towers in the inversion estimation. We note that more data may be more effective in reducing uncertainty in SFBA fFCO₂ emissions if transport model bias errors are <10%, as suggested by the evaluation of modeled wind speed and wind direction described by Bagley et al., 2017.

The inversion analysis using the combined measurements from SBC and CIT for June 2013 to May 2014 obtains posterior emissions of 124 ± 31 Tg CO₂/yr at 95% confidence in SoCAB, which are within $13 \pm 28\%$ of prior emissions for the region. Contrasting with the SFBA, SoCAB emissions appear marginally higher in summer than in other seasons,

Table 5

Posterior fFCO₂ emissions in SoCAB (posterior uncertainty at 95% confidence) from all prior maps listed in first column based on seasonal inversions for southern California (prior uncertainty = 0.25; factor for the R matrix = 0.5; ocean cut used).

Prior maps	Posterior emission (unit = Tg CO ₂ /yr)
Scaled Vulcan map	124 ± 31
Original Vulcan map	121 ± 30
Annual original Vulcan map	122 ± 31
EDGAR map	123 ± 31
50% Scaled Vulcan map	81 ± 22
200% Scaled Vulcan map	130 ± 36
Flat Flux map	79 ± 82

consistent with the work of Newman et al. (2016). However, detection of any significant seasonality would likely require more observations. Different from the SFBA region, the seasonal variations of ffCO₂ emissions in SoCAB are contributed by more sources from the Vulcan 2.2 prior map such as transportation, residential usage and power production, thus future source inversions will require more tracers, such as CH₄, CO, and others.

With respect to additional potential sources of error, we speculate that inadequate spatial resolution in the Vulcan emission map may contribute to aggregation error in the model-data mismatch (**R**) matrix. For example, Feng et al., 2016 show the RMSE of ffCO₂ between the WRF-Vulcan (1.3-km resolution map derived from the 10-km Vulcan map) predictions and in-situ measurements at Pasadena site is 5.51 ppm which is slightly smaller than 6.21 ppm for WRF-Hestia (1.3 km resolution) modeling. However, uncertainties in the spatial distribution of ffCO₂ may increase at smaller scales (Hogue et al., 2016). Emissions in Vulcan tend to be less concentrated in urban regions compared to other emissions estimates such as EDGAR (Brophy et al., 2018). Here, simulated inversion experiments in California using the same measurement network as in Graven et al., 2018 found that posterior estimates of emissions obtained using the EDGAR prior were consistently lower (although not significantly different) than those obtained using the Vulcan prior (Brophy et al., 2018).

In conclusion, the inversions reported here provide annually averaged estimates of urban ffCO₂ emissions for SFBA over the 2009–2012 period and SoCAB over the June 2013–May 2014 period. Together these regions comprise ~50% of total emissions in California. Further work including Δ¹⁴CO₂ observations at more sites across California is expected to improve estimates of fossil fuel CO₂ emissions in California.

Acknowledgements

We thank David Field, Dave Bush, Edward Wahl, Ken Reichl, Toby Walpert, and particularly Jon Kofler for assistance with measurements at WGC, John Lin, Christoph Gerbig, Steve Wofsy, Janusz Eluszakiewicz, Thomas Nehrkorn for sharing the STILT code and advice, and Krishna Muriki for assistance running the WRF-STILT models on the LBNL-Lawrencium cluster. WGC 14C measurements were supported by NOAA-OGP awards to Scott Lehman and John Miller. This study was in part supported by the CARB Research Division (CARB contract 11-306) under U.S. Department of Energy contract DE-AC02-05CH11231. The statements and conclusions in this article are those of the authors and not necessarily those of the California Air Resources Board. The mention of commercial products, their source, or their use in connection with material reported herein is not to be construed as actual or implied endorsement of such products. The views and opinions of authors expressed herein do not necessarily state or reflect those of the United States Government or any agency thereof, or The Regents of the University of California. Ernest Orlando Lawrence Berkeley National Laboratory is an equal opportunity employer. WGC measurement data are available through <https://www.esrl.noaa.gov/gmd/ccgg/flask.php>, and data for CARB sites are available at <https://www.arb.ca.gov/aqmis2/res/aqdselect.php?tab=hourly>. The EDGAR and CARB prior emissions are available at <http://edgar.jrc.ec.europa.eu> and <https://www.arb.ca.gov/cc/inventory/inventory.htm>, respectively.

Appendix A. Supplementary data

Supplementary data to this article can be found online at <https://doi.org/10.1016/j.scitotenv.2019.01.081>.

References

Andrews, A.E., Kofler, J.D., Trudeau, M.E., Williams, J.C., Neff, D.H., Masarie, K.A., Chao, D.Y., Kitzis, D.R., Novelli, P.C., Zhao, C.L., Dlugokencky, E.J., Lang, P.M., Crotwell, M.J., Fischer, M.L., Parker, M.J., Lee, J.T., Baumann, D.D., Desai, A.R., Stanier, C.O., De Wekker, S.F.J., Wolfe, D.E., Munger, J.W., Tans, P.P., 2014. CO₂, CO, and CH₄ measurements from tall towers in the NOAA earth system research laboratory's global greenhouse gas reference network: instrumentation, uncertainty analysis, and recommendations for future high-accuracy greenhouse gas monitoring efforts. *Atmos. Meas. Tech.* 7, 647–687. <https://doi.org/10.5194/amt-7-647-2014>.

Bagley, J., Jeong, S., Cui, X.G., Newman, S., Zhang, J.S., Priest, C., Campos-Pineda, M., Andrews, A., Bianco, L., Lloyd, M., Lareau, N., Clements, C., Fischer, M., 2017. Assessment of an atmospheric transport model for annual inverse estimates of California greenhouse gas emissions, journal of geophysical research. *Atmospheres* 122, 1901–1918. <https://doi.org/10.1002/2016JD025361>.

Basu, S., Miller, J.B., Lehman, S., 2016. Separation of biospheric and fossil fuel fluxes of CO₂ by atmospheric inversion of CO₂ and 14CO₂ measurements: observation system simulations. *Atmos. Meas. Tech.* 16 (9), 5665–5683. <https://doi.org/10.5194/acp-16-5665-2016>.

Bergamaschi, P., Krol, M., Dentener, F., Vermeulen, A., Meinhardt, F., Graul, R., Ramonet, M., Peters, W., Dlugokencky, E.J., 2005. Inverse modelling of national and European CH₄ emissions using the atmospheric zoom model TM5. *Atmos. Chem. Phys.* 5, 2431–2460.

Bianco, L., Djalalova, I.V., King, C.W., Wilczak, J.M., 2011. Diurnal evolution and annual variability of boundary-layer height and its correlation to other meteorological variables in California's Central Valley. *Bound.-Layer Meteorol.* 140 (491–511), 1–21. <https://doi.org/10.1007/s10546-011-9622-4>.

Brioude, J., et al., 2013. Top-down estimate of surface flux in the Los Angeles Basin using a mesoscale inverse modeling technique: assessing anthropogenic emissions of CO, NO_x and CO₂ and their impacts. *Atmos. Chem. Phys.* 13 (7), 3661–3677.

Brophy, K., Graven, H., Manning, A.J., White, E., Arnold, T., Fischer, M.L., Jeong, S., Cui, X., Rigby, M., 2018. Characterizing uncertainties in atmospheric inversions of fossil fuel CO₂ emissions in California. *Atmos. Chem. Phys.* <https://doi.org/10.5194/acp-2018-473>.

CARB, 2014. California greenhouse gas emissions inventory. California Air Resources Board Staff Report. Available at: <http://www.arb.ca.gov/cc/inventory/inventory.htm>, Accessed date: January 2015 version March 2014.

CARB, 2016. California Greenhouse Gas Emissions Inventory. California Air Resources Board Staff Report. <http://www.arb.ca.gov/cc/inventory/inventory.htm>, Accessed date: February 2017 version June 2016.

de la Rue du Can, S., Price, L., 2008. Sectoral trends in global energy use and greenhousegas emissions. *Energy Policy* (ISSN: 0301-4215) 36 (4), 1386–1403. <https://doi.org/10.1016/j.enpol.2007.12.017>.

EDGAR4.2, 2015. European Commission, Joint Research Centre (JRC)/Netherlands Environmental Assessment Agency (PBL). Emission Database for Global Atmospheric Research (EDGAR). release version 4.2. <http://edgar.jrc.ec.europa.eu>.

Etheridge, D.M., Steele, L.P., Langenfelds, R.L., Francey, R.J., Barnola, J.M., Morgan, V.I., 1996. Natural and anthropogenic changes in atmospheric CO₂ over the last 1000 years from air in Antarctic ice and firn. *J. Geophys. Res.-Atmos.* 101, 4115–4128.

Feng, S., Lauvaux, T., Newman, S., Rao, P., Ahmadov, R., Deng, A., Diaz-Isaac, L.I., Duren, R.M., Fischer, M.L., Gerbig, C., Gurney, K.R., Huang, J., Jeong, S., Li, Z., Miller, C.E., O'Keeffe, D., Patarasuk, R., Sander, S.P., Song, Y., Wong, K.W., Yung, Y.L., 2016. Los Angeles megacity: a high-resolution land-atmosphere modelling system for urban CO₂ emissions. *Atmos. Chem. Phys.* 16 (14), 9019–9045. <https://doi.org/10.5194/acp-16-9019-2016>.

Fischer, M.L., Parazoo, N., Brophy, K., Cui, X.G., Jeong, S., Liu, J., Keeling, R., Taylor, T.E., Gurney, K., Oda, T., Graven, H., 2017. Simulating estimation of California fossil fuel and biosphere carbon dioxide exchanges combining in-situ tower and satellite column observations. *J. Geophys. Res.-Atmos.* 122. <https://doi.org/10.1002/2016JD025617>.

Gerbig, C., Lin, J., Wofsy, S., Daube, B., Andrews, A.E., Stephens, B., Bakwin, P.S., Grainger, C., 2003. Toward constraining regional-scale fluxes of CO₂ with atmospheric observations over a continent: 2. Analysis of CO₂ data using a receptor-oriented framework. *J. Geophys. Res.-Atmos.* 108 (D24). <https://doi.org/10.1029/2003JD003770>.

Göckede, M., Michalak, A.M., Vickers, D., Turner, D.P., Law, B.E., 2010. Atmospheric inverse modeling to constrain regional-scale CO₂ budgets at high spatial and temporal resolution. *J. Geophys. Res.-Atmos.* 115, D15113. <https://doi.org/10.1029/2009JD012257>.

Graven, H.D., Guilderson, T.P., Keeling, R.F., 2012. Observations of radiocarbon in CO₂ at seven global sampling sites in the Scripps flask network: analysis of spatial gradients and seasonal cycles. *J. Geophys. Res.-Atmos.* 117, D02303. <https://doi.org/10.1029/2011JD016535>.

Graven, H., Fischer, M.L., Lueker, T., Jeong, S., Guilderson, T.P., Keeling, R.F., Bambha, R., Brophy, K., Callahan, W., Cui, X., Frankenberg, C., LaFranchi, B.W., Lehman, S., Michelsen, H., Miller, J.B., Newman, S., Paplawsky, W., Parazoo, N.C., Sloop, C., Walker, S.J., 2018. Assessing fossil fuel CO₂ emissions in California using atmospheric observations and models. *Environ. Res. Lett.* <https://doi.org/10.1088/1748-9326/ab4d43>.

Gurney, K., Mendoza, D., Zhou, Y., Fischer, M.L., Miller, C., Geethakumar, S., du Can, S., 2009. High resolution fossil fuel combustion CO₂ emission fluxes for the United States. *Environ. Sci. Technol.* 43, 5535–5541.

Gurney, K.R., Razlivanov, I., Song, Y., Zhou, Y., Benes, B., Abdul-Massih, M., 2012. Quantification of fossil fuel CO₂ emissions on the building/street scale for a large U.S. City. *Environ. Sci. Technol.* 46, 12194–12202.

Hogue, S., Marland, E., Andres, R.J., Marland, G., Woodard, D., 2016. Uncertainty in gridded CO₂ emissions estimates. *Earth's Future* 4 (5), 225–239. <https://doi.org/10.1002/2015EF000343>.

IPCC, 2013. Climate change: the physical science basis. In: Stocker, T.F., et al. (Eds.), Contribution of Working Group I to the Fifth Assessment Report of the Intergovernmental Panel on Climate Change. Cambridge University Press, Cambridge, United Kingdom and New York, NY, USA. 1535 pp. <https://www.ipcc.ch/report/ar5/>.

Jeong, S., Zhao, C., Andrews, A.E., Bianco, L., Wilczak, J.M., Fischer, M.L., 2012a. Seasonal variation of CH₄ emissions from Central California. *J. Geophys. Res.-Atmos.* 117 (D11).

Jeong, S., Zhao, C., Andrews, A.E., Dlugokencky, E.J., Sweeney, C., Bianco, L., Wilczak, J.M., Fischer, M.L., 2012b. Seasonal variations in N₂O emissions from central California. *Geophys. Res. Lett.* 39, L16805.

Jeong, S., Hsu, Y.-K., Andrews, A.E., Bianco, L., Vaca, P., Wilczak, J.M., Fischer, M.L., 2013. A multitower measurement network estimate of California's methane emissions. *J. Geophys. Res.-Atmos.* 118, 339–351.

Jeong, S., Newman, S., Zhang, J., Andrews, A.E., Bianco, L., Bagley, J., Cui, X.G., Graven, H., Kim, J., Salameh, P., LaFranchi, B.W., Priest, C., Campos-Pineda, M., Novakovskia, E., Sloop, C.D., Michelsen, H.A., Bambha, R.P., Weiss, R.F., Keeling, R., Fischer, M.L., 2016. Estimating methane emissions in California's urban and rural regions using multitower observations. *J. Geophys. Res.-Atmos.* 121 (13), 031–13,049. <https://doi.org/10.1002/2016JD025404>.

Jeong, S., Cui, Xinguang, Blake, Donald R., Miller, Ben, Montzka, Stephen A., Andrews, Arlyn, Guha, Abhinav, Martien, Philip, Bambha, Ray P., LaFranchi, Brian, Michelsen, Hope A., Clements, Craig B., Glaise, Pierre, Fischer, Marc L., 2017. Estimating methane emissions from biological and fossil-fuel sources in the San Francisco Bay Area. *Geophys. Res. Lett.* 44, 486–495. <https://doi.org/10.1002/2016GL071794>.

Jeong, S., Newman, S., Zhang, J.S., Andrews, A., Bianco, L., Dlugokencky, E., Bagley, J., Cui, X.G., Priest, C., Campos-Pineda, M., Fischer, M., 2018. Inverse estimation of an annual cycle of California's nitrous oxide emissions. *J. Geophys. Res.-Atmos.* 123, 4758–4771. <https://doi.org/10.1029/2017JD028166>.

Kort, E.A., Angevine, W., Duren, R., Miller, C.E., 2013. Surface observations for monitoring urban fossil fuel CO₂ emissions (2013). Minimum site location requirements for the Los Angeles megacity. *J. Geophys. Res.-Atmos.* 118 (3), 1577–1584. <https://doi.org/10.1002/jgrd.50135>.

Legislative Information, 2006. Assembly Bill AB32, Official California Legislative Information, 27 September, from. http://www.leginfo.ca.gov/pub/05-06/bill/asm/ab_0001-0050/ab_32_bill_20060927_chaptered.html, Accessed date: May 2017.

Lehman, S., Miller, J., Wolak, C., Southon, J., Tans, P., Montzka, S., Sweeney, C., Andrews, A., LaFranchi, B., Guilderson, T., Turnbull, J., 2013. Allocation of terrestrial carbon sources using ¹⁴CO₂: methods, measurement, and modeling. *Radiocarbon* 55 (3), 1484–1495. <https://doi.org/10.1017/S0033822200048414>.

Levin, I., Roedenbeck, C., 2008. Can the envisaged reductions of fossil fuel CO₂ emissions be detected by atmospheric observations? *Naturwissenschaften* 95 (3), 203–208. <https://doi.org/10.1007/s00114-007-0313-4>.

Lin, J.C., Gerbig, C., Wofsy, S.C., Andrews, A.E., Daube, B.C., Davis, K.J., Grainger, C.A., 2003. A near-field tool for simulating the upstream influence of atmospheric observations: the stochastic time-inverted Lagrangian transport (STILT) model. *J. Geophys. Res. Atmos.* 108 (D16), 4493. <https://doi.org/10.1029/2002JD003161>.

McKain, K., Down, A., Raciti, S.M., Budney, J., Hutyra, L.R., Floerchinger, C., Herndon, S.C., Nehrkorn, T., Zahniser, M.S., Jackson, R.B., Phillips, N., Wofsy, S.C., 2015. Methane emissions from natural gas infrastructure and use in the urban region of Boston, Massachusetts. *Proc. Natl. Acad. Sci.* 112 (7), 1941–1946. <https://doi.org/10.1073/pnas.1416261112>.

Mesinger, F., DiMego, G., Kalnay, E., Mitchell, K., Shafran, P.C., Ebisuzaki, W., Jović, D., Woolen, J., Rogers, E., Berbery, E.H., Ek, M.B., Fan, Y., Grumbine, R., Higgins, W., Li, H., Lin, Y., Manikin, G., Parrish, D., Shi, W., 2006. North American regional reanalysis. *Bull. Am. Meteorol. Soc.* 87 (3), 343–360.

Miller, J.B., Lehman, S.J., Montzka, S.A., Sweeney, C., Miller, B.R., Karion, A., Wolak, C., Dlugokencky, Ed J., Southon, J., Turnbull, J.C., Tans, P.P., 2012. Linking emissions of fossil fuel CO₂ and other anthropogenic trace gases using atmospheric ¹⁴CO₂. *Mon. Weather Rev.* 117, D08302. <https://doi.org/10.1029/2011JD017048>.

National Research Council, 2010. Verifying greenhouse gas emissions: methods to support international climate agreements. *Natl. Acad. Press, Washington, D. C.*

Nehrkorn, T., Eluszkiewicz, J., Wofsy, S.C., Lin, J.C., Gerbig, C., Longo, M., Freitas, S., 2010. Coupled weather research and forecasting - stochastic time-inverted lagrangian transport (WRF-STILT) model. *Meteorol. Atmos. Phys.* 107 (1), 51–64. <https://doi.org/10.1007/s00703-010-0068-x>.

Newman, S., Xu, X., Affek, H.P., Stolper, E., Epstein, S., 2008. Changes in mixing ratio and isotopic composition of CO₂ in urban air from the Los Angeles basin, California, between 1972 and 2003. *J. Geophys. Res.-Atmos.* 113, D23304. <https://doi.org/10.1029/2008JD009999>.

Newman, S., Jeong, S., Fischer, M.L., Xu, X., Haman, C.I., Lefer, B., Alvarez, S., Rappenglueck, B., Kort, E.A., Andrews, A.E., Peischl, J., Gurney, K.R., Miller, C.E., Yung, Y.L., 2013. Diurnal tracking of anthropogenic CO₂ emissions in the Los Angeles basin megacity during spring 2010. *Atmos. Chem. Phys.* 13 (8), 4359–4372. <https://doi.org/10.5194/acp-13-4359-2013>.

Newman, S., Xu, X., Gurney, K.R., Hsu, Y.K., Li, K.F., Jiang, X., Keeling, R., Feng, S., O'Keefe, D., Patarasuk, R., Wong, K.W., Rao, P., Fischer, M.L., Yung, Y.L., 2016. Toward consistency between trends in bottom-up CO₂ emissions and top-down atmospheric measurements in the Los Angeles megacity. *Atmos. Chem. Phys.* 16, 3843–3863. <https://doi.org/10.5194/acp-16-3843-2016>.

NOAA, 2018. Trends in Atmospheric Carbon Dioxide. National Oceanic and Atmospheric Administration <https://www.esrl.noaa.gov/gmd/ccgg/trends/full.html>, Accessed date: April 2018.

Pataki, D.E., Bowling, D.R., Ehleringer, J.R., 2003. Seasonal cycle of carbon dioxide and its isotopic composition in an urban atmosphere: anthropogenic and biogenic effects, journal of geophysical research. *Atmospheres* 108 (D23), 4735. <https://doi.org/10.1029/2003JD003865>.

PG&E, 2016. Online Reporting of Natural Gas Composition. http://www.pge.com/pipeline/operations/gas_quality/index.page (accessed January–December, 2016).

Skamarock, W.C., Klemp, J.B., Dudhia, J., Gill, D.O., Barker, D.M., Huang, X.Z., Wang, W., Powers, J.G., 2008. A Description of the Advanced Research WRF Version 3. Technical Note 475+STR. Mesoscale and Microscale Meteorology Division, NCAR, Boulder, Colorado.

Tarantola, A., 1987. *Inverse Problem Theory Methods for Data Fitting and Model Parameter Estimation*. 613. Elsevier, New York.

Turnbull, J., Miller, J., Lehman, S., Tans, P., Sparks, R., Southon, J., 2006. Comparison of ¹⁴CO₂, CO, and SF₆ as tracers for recently added fossil fuel CO₂ in the atmosphere and implications for biological CO₂ exchange. *Geophys. Res. Lett.* 33 (1), L01817.

Turnbull, J.C., Karion, A., Fischer, M.L., Faloona, I., Guilderson, T., Lehman, S.J., Miller, B.R., Miller, J.B., Montzka, S., Sherwood, T., Saripalli, S., Sweeney, C., Tans, P.P., 2011. Assessment of fossil fuel carbon dioxide and other anthropogenic trace gas emissions from airborne measurements over Sacramento, California in spring 2009. *Atmos. Chem. Phys.* 11 (2), 705–721. <https://doi.org/10.5194/acp-11-705-2011>.

Turnbull, J., Sweeney, C., Karion, A., Newberger, T., Tans, P., Lehman, S., Davis, K.J., Miles, N.L., Richardson, S.J., Lauvaux, T., Cambaliza, M.O., Shepson, P., Gurney, K.R., Song, Y., Razlivanova, I., Zondervan, A., 2015. Towards quantification of fossil fuel CO₂ and trace gas emissions from an urban area: results from the INFLUX experiment, journal of geophysical research. *Atmospheres* 120, 292–312. <https://doi.org/10.1002/2014JD02255>.

Turner, A.J., Jacob, D.J., Wecht, K.J., Maasakkers, J.D., Lundgren, E., Andrews, A.E., Biraud, S.C., Boesch, H., Bowman, K.W., Deutscher, N.M., Dubey, M.K., Griffith, D.W.T., Hase, F., Kuze, A., Notholt, J., Ohyama, H., Parker, R., Payne, V.H., Sussmann, R., Sweeney, C., Velazco, V.A., Warneke, T., Wennberg, P.O., Wunch, D., 2015. Estimating global and North American methane emissions with high spatial resolution using GOSAT satellite data. *Atmos. Chem. Phys.* 15 (12), 7049–7069.

UN: World Urbanization Prospects e Revision, 2005. Factsheet 7: Mega-cities, 2006, United Nations, Department of Economic and Social Affairs, Population Division. *World Urbanization Prospects: The 2005 Revision*, Working Paper No. ESA/P/WP/200. Technology report. 2006.

Wecht, K.J., Jacob, D.J., Sulprizio, M.P., Santoni, G.W., Wofsy, S.C., Parker, R., Bösch, H., Worden, J., 2014. Spatially resolving methane emissions in California: constraints from the CalNex aircraft campaign and from present (GOSAT, TES) and future (TROPOMI, geostationary) satellite observations. *Atmos. Chem. Phys.* 14, 8173–8184. <https://doi.org/10.5194/acp-14-8173-2014>.

Welch, B.L., 1947. The generalization of "Student's" problem when several different population variances are involved. *Biometrika* 34 (1–2), 28–35.

Xu, X., Trumbore, S.E., Zheng, S., Southon, J.R., McDuffee, K.E., Lutgen, M., Liu, J.C., 2007. Modifying a Sealed Tube Zinc Reduction Method for Preparation of AMS Graphite Targets: Reducing Background and Attaining High Precision. 259 pp. 320–329.

Zhao, C., Andrews, A.E., Bianco, L., Eluszkiewicz, J., Hirsch, A., MacDonald, C., Nehrkorn, T., Fischer, M.L., 2009. Atmospheric inverse estimates of methane emissions from Central California. *J. Geophys. Res. Atmos.* 114, D16302. <https://doi.org/10.1029/2008JD011671>.